International Journal of Heat and Mass Transfer 172 (2021) 121171

Contents lists available at ScienceDirect

International Journal of Heat and Mass Transfer

journal homepage: www.elsevier.com/locate/hmt

Multiple wall temperature peaks during forced convective heat transfer of supercritical carbon dioxide in tubes

Haisong Zhang[a], Jinliang Xu[a,b], Qingyang Wang[a,b,*], Xinjie Zhu[a]

[a] Beijing Key Laboratory of Multiphase Flow and Heat Transfer for Low Grade Energy Utilization, North China Electric Power University, Beijing 102206, China

[b] Key Laboratory of Power Station Energy Transfer Conversion and System, North China Electric Power University, Ministry of Education, Beijing, 102206, China

ARTICLE INFO

Article history:
Received 25 October 2020
Revised 14 January 2021
Accepted 28 February 2021

Keywords:
Supercritical fluid
Heat transfer deterioration
Pseudo-boiling
Multi-peak
Supercritical boiling number

ABSTRACT

Heat transfer deterioration (HTD) is defined as having one or multiple wall temperature peaks along the flow length for supercritical heat transfer. The single-peak phenomenon has been widely reported in the literature, but the multi-peak phenomenon is seldomly studied and not well understood. Here, the convective heat transfer of supercritical carbon dioxide in vertical tubes is investigated, with pressure, mass flux, and heat flux in the ranges of 7.5~23 MPa, 400~1500 kg/m^{2}s, and 25~450 kW/m^2, respectively, and inner tube diameter covering 8, 10, and 12 mm. Sudden changes are observed between normal heat transfer (NHT) without wall temperature peak and HTD by crossing a global critical supercritical boiling number (*SBO*) based on the pseudo-boiling theory. For HTD, we show that inner diameter and pressure have significant influences on whether the multi-peak phenomenon occurs: it takes place for inner diameter of 12 mm only and under pressure of ~8 and ~12.5 MPa. It is found that friction factors for multi-peak cases are obviously larger than those for single-peak or NHT cases, which is successfully explained by the orifice contraction effect due to the strong “vapor” expansion at the tube cross-section corresponding to the sharp wall temperature peak. The multi-peak phenomenon is shown to be governed by the competition between the local evaporation momentum force and inertia force along the flow length. Our work enhances the understanding of supercritical heat transfer and verifies the validity of pseudo-boiling assumption, and can also benefit engineering applications in advanced power cycles.

1. Introduction

Supercritical fluid has been widely used in a variety of applications, including food processing, pharmaceutics, materials synthesis, micro/nano systems, refrigeration, and power generation [1-3]. In particular, in power engineering, increasing temperature and pressure can increase the cycle efficiency, which makes supercritical cycles attractive for advanced power generation systems [4,5]. Advanced ultra-supercritical power generation technology using water has been commercialized and shown to achieve high efficiency of ~47% [6]. Recently, supercritical CO_2 power generation is being extensively studied and has great potential as a more efficient and safer technology to replace water cycles [7-9], which can use various types of energy sources such as nuclear, solar, waste heat, or fossil fuels [10-12]. Understanding the heat transfer of supercritical fluid is of great importance for supercritical power cycles to improve system design and ensure system safety.

In heat transfer of supercritical fluid, a hazardous phenomenon called “heat transfer deterioration” (HTD) is widely observed, which shows a substantial wall temperature rise [13-15]. When HTD does not occur, the heat transfer is either normal or enhanced, which is grouped together in this work and called the “normal heat transfer” (NHT) mode. Since there is no liquid-vapor phase transition at supercritical pressures, supercritical heat transfer is commonly analyzed by treating the fluid as single-phase. Hence, the occurrence of HTD is attributed to the variation of thermophysical properties and the buoyancy/acceleration effect [16,17]. However, the criteria based on buoyancy and acceleration effects can not accurately predict supercritical heat transfer [16,18]. Table 1 lists the criteria reported in the literature for HTD in vertical tubes for various supercritical fluids [19-24]. The reason causing the discrepancies between experimental data and the criteria is that in the derivation of these criteria, the single-phase assumption for supercritical fluid is applied, which neglects the practical pseudo-two-phase effect. Moreover, these criteria are based on the two-region model, which requires an appropriate characteristic temperature, and the validity of the model is highly dependent on the

* Corresponding author:
E-mail address: wangqy@ncepu.edu.cn (Q. Wang).

https://doi.org/10.1016/j.ijheatmasstransfer.2021.121171

Nomenclature

A	area, m^2
Ac	non-dimensional flow acceleration parameter
Bo	boiling number
Bu	non-dimensional buoyancy parameter
c_p	specific heat at constant pressure, J/kg K
C_{ac}	constant
d	tube diameter, m
f	friction coefficient
F	force per unit area, N/m^2
g	gravitational acceleration, m/s^2
G	mass flux, kg/m^2s
Gr	Grashof number
h	heat transfer coefficient, W/m^2K
i	enthalpy, J/kg
I	current, A
K	non-dimensional parameter representing evaporation induced momentum force relative to inertia force
L	length, m
m	mass flow rate, kg/s
n	number of peaks
P	pressure, Pa
P_c	actual heating power, W
P_e	total electric heating power, W
q	heat flux, W/m^2
q"	"interfacial evaporation" heat flux, W/m^2
q^+	non-dimensional heat flux
r	radius, m
T	temperature, °C
ΔT	wall temperature rise, °C
u	mean velocity, m/s
U	voltage, V
z	axial coordinate, m

Greek symbols

λ	thermal conductivity, W/mK
ρ	density, kg/m^3
η	efficiency
μ	dynamic viscosity, Pa s
β	volume expansion coefficient, 1/K

Subscripts

ac	acceleration
ave	average
b	bulk fluid
c	cross section
cr	critical
f	friction
fg	saturation vapor-liquid
g	gravity
GL	gas-like
I'	inertia
i	inner
in	inlet
l	liquid
LL	liquid-like
M'	momentum
o	outer
out	outlet
pc	pseudocritical
th	thermal
v	vapor
w	inner wall

Acronyms

DC	direct current
HTD	heat transfer deterioration
NHT	normal heat transfer
SBO	supercritical boiling number
WL	Widom line

wall heat flux. Besides theoretical analysis and experimental investigation, attempts have also been made by researchers to study supercritical heat transfer using numerical methods. The SST k-ω and low-Re k-ε turbulence models are found to be applicable for NHT regime, but for HTD regime, they can only qualitatively predict wall temperature variations and cannot capture the unique features, especially the wall temperature recovery in HTD [25]. Thus, the pseudo-two-phase effect of supercritical fluid started to be paid attention to, and direct numerical simulation method has been explored to study supercritical heat transfer. Peeters et al. [26] used direct numerical simulation method to study supercritical CO_2 heat transfer in an annulus. They found that HTD can still happen in supercritical heat transfer even when there is no buoyancy or acceleration effect, and the low density fluid near the high temperature wall has significant effect on heat transfer. Kim et al. [27] simulated the pseudo-phase change process of supercritical R134a using direct numerical simulation. By controlling the temperatures of the two walls, the pseudocritical temperature is maintained in between the wall temperatures. The authors found that the thickness of the fluid layer undergoing pseudo-phase change decreases with increasing temperature difference between the two walls. Recently, the different features between liquid-like and gas-like phases in supercritical fluid have gradually been considered in analyzing supercritical heat transfer. Using inelastic X-ray scattering and molecular dynamics simulations, Simeoni et al. [28] discovered sharp transition of acoustic behavior in supercritical fluid when crossing the Widom line (WL). By analyzing the thermody-

Table 1
Representative deterioration criteria for vertical tubes in the literatures.

Reference	Criteria	Fluid	Mechanism
Shiralkar and Griffith [19]	$Bu = \frac{Gr_b}{{Re_b}^2}$	CO_2	buoyancy
Jackson et al. [20]	$Bu = \frac{Gr_b}{{Re_b}^{2.7}}$	-	buoyancy
Jackson et al. [21]	$Bu = \frac{Gr_q}{Re^{3.425}Pr^{0.8}}$	H_2O	buoyancy
Liu et al. [22]	$Bu = \frac{Gr_b}{{Re_b}^{2.625}{Pr_w}^{0.4}}\left(\frac{\rho_b}{\rho_w}\right)^{0.5}\left(\frac{\mu_w}{\mu_b}\right)$	CO_2	buoyancy
Kim and Kim [23]	$Bu = \frac{Gr_q}{Re_b^{3.425}Pr_b^{0.8}}\left(\frac{\rho_b}{\rho_w}\right)^{0.5}\left(\frac{\mu_w}{\mu_b}\right)$	CO_2	buoyancy
McEligot et al. [24]	$Ac = \frac{4q_w d\beta_b}{Re^2\mu_b c_{p,b}} = \frac{q^+}{Re^2}$	Gas	acceleration
Kim and Kim [23]	$Ac = C_{ac}\frac{q_w\beta_b}{Gc_{p,b}Re_b^{0.625}}\left(\frac{\mu_w}{\mu_b}\right)\left(\frac{\rho_b}{\rho_w}\right)^{0.5}$	CO_2	acceleration
Liu et al. [22]	$Ac = \frac{4q_w}{Gc_{p,b}T_bRe_b^{0.625}}\left(\frac{\mu_w}{\mu_b}\right)\left(\frac{\rho_b}{\rho_w}\right)^{0.5}$	CO_2	acceleration

namic properties of supercritical water, Gallo et al. [29] identified liquid-like and gas-like phases divided by the WL. Banuti [30] theoretically demonstrated the existence of pseudo-boiling under supercritical pressures in analogous to boiling under subcritical pressures, and proposed a new equation for the pseudo-boiling line. Maxim [31] used neutron imaging technique and visualized the density fluctuations of supercritical water from liquid-like to gas-like when crossing the WL, which is consistent with the pseudo-boiling theory proposed by Banuti [30]. Moreover, although surface tension vanishes in supercritical fluid under thermal equilibrium condition, it can exist when there is a temperature gradient [32], which further enables the analogy between supercritical heat transfer and subcritical boiling and validates the pseudo-boiling concept.

The literature survey can be summarized as follows: (1) The criteria for HTD proposed based on the single-phase assumption and buoyancy/acceleration effect are only suitable for their own experimental conditions and not widely applicable. (2) Numerical models and methods which can accurately simulate HTD of supercritical fluid are still lacking. (3) The qualitative and quantitative similarities of supercritical heat transfer with subcritical boiling need to be paid attention to, due to the vastly different dynamic and thermodynamic behaviors of the liquid-like and gas-like phases [28,29]. Hence, using single-phase assumption to analyze supercritical heat transfer is facing great challenges.

Therefore, a series of studies have been performed by Xu's group [33-37], aiming to use the pseudo-boiling theory to understand heat transfer of supercritical fluid. Zhu et al. [33] experimentally studied heat transfer of supercritical CO_2 flowing upward inside a heated tube with 10 mm inner diameter. The authors defined a supercritical boiling number (*SBO*) based on subcritical boiling theory, and showed that *SBO* is the critical parameter to distinguish NHT and HTD, with the critical *SBO* being 5.126×10^{-4} for supercritical CO_2. The reason for HTD was attributed to the expansion and growth of the "vapor film" near the wall. Xu et al. [34] further extended the experimental investigations to supercritical H_2O, R134a, and R22, and identified the different critical *SBO*s for these fluids. Zhu et al. [35] studied supercritical CO_2 heat transfer inside a tube with non-uniform heating, and showed that *SBO* is also useful in determining the onset of HTD under non-uniform heating condition. The critical *SBO* for non-uniform heating is found to be 8.908×10^{-4} which indicates that non-uniform heating can suppress the onset of HTD. Zhu et al. [36] performed analogy between supercritical heat transfer and subcritical boiling. Using the experimental database containing results for CO_2, H_2O, and R134, the authors proposed a heat transfer correlation using the supercritical *K* number, and demonstrated that the correlation is applicable for a wide range of working fluids and experimental conditions including both NHT and HTD regimes. Zhang et al. [37] further studied the linkage between heat transfer and pressure drop of supercritical flow in tubes. They found that when HTD occurs, the frictional pressure drop also increases due to the orifice contraction effect, and a larger *SBO* corresponds to a larger friction factor. They further proposed a correlation for friction factor using the *K* number, which is suitable for both NHT and HTD regimes.

For supercritical fluid flowing inside a heated tube, the HTD regime is associated with temperature peaks in the temperature profile along the tube. However, most or the previous studies on HTD either only reported one peak case or did not distinguish different types of deterioration in HTD regime. Only a few papers showed multiple peaks. Bourke et al. [38] experimentally studied heat transfer of supercritical CO_2, and observed two peaks in wall temperature profile under low mass flow rate, with the second one being broader than the first one. Ackerman [39] observed two peaks in the experiments with supercritical water. Jackson et al. [40] conducted experiments on supercritical CO_2 flow at pressures just below and just above the critical pressure, and observed two or three peaks under supercritical pressures. However, all these authors only provided simple descriptions of the multi-peak phenomenon, and the reasons causing the phenomenon were not discussed. Cheng et al. [41] numerically studied the two-peak phenomenon using SST k-ω turbulence model. The occurrence of the first and second peaks was attributed to buoyancy effect and shear stress, respectively, both of which causes flattened velocity profile and reduction of turbulent kinetic energy. However, the model did not well capture the wall temperature variation and can only provide qualitative description of HTD.

Based on the literature survey mentioned above, although the multi-peak phenomenon has been observed in the literature, it was not systematically studied, and the underlying mechanisms were not discussed. Thus, the objective of this work is to experimentally study the multi-peak phenomenon of supercritical CO_2 heat transfer, to discuss the effects of various parameters on the multi-peak phenomenon, and to understand the mechanisms based on pseudo-boiling theory. Experiments were conducted for supercritical CO_2 flowing upward in heated vertical tubes, with a wide range of working conditions and different tube diameters. Variation of tube diameter is shown to affect the heat transfer characteristics: the heat transfer coefficient increases with decreasing tube diameter due to the larger velocity gradient near the wall. However, variation of tube diameter does not affect the onset of HTD: the critical *SBO* distinguishing NHT and HTD regimes are found to be relatively unchanged with different diameters. Three different modes are observed in HTD regime: single-peak, two-peak, and three-peak. The multi-peak phenomenon only occurs in large tube diameter and under low pressure, due to the large temperature rise which causes the formation of a thick "vapor film". Multi-peak cases demonstrate higher friction factor than single-peak cases, which is attributed to the existence of multiple orifices along the tube which contracts the fluid multiple times. The oscillations of "vapor film" thickness and wall temperature are resulted from the alternating dominance of local evaporation momentum force and local inertia force. Our work can lead to a better understanding of the underlying mechanisms of supercritical heat transfer and will benefit future application of supercritical fluid in advanced power cycles.

2. Experimental

2.1. Experimental system

Fig. 1 shows the schematic of the experimental system used in this work, which is the same one used in Ref. [37]. The system consists of a CO_2 circulation loop, a coolant circulation loop, and an electric heating system. The maximum allowable pressure and temperature of the loop are 25 MPa and 500 °C, respectively. High purity (>99.9%) CO_2 is used as the working fluid. Before formal experiments, the CO_2 circulation loop is vacuumed to remove non-condensable gas, and high purity CO_2 is then charged into the loop. The CO_2 circulation loop is driven by a high pressure, low temperature plunger supercritical CO_2 pump, which has two pathways: a main loop through the test section, and a bypass. After passing through the pump, CO_2 flow in the main loop passes through an accumulator to reduce flow rate and pressure surges caused by the plunger pump, flows through one of the two Coriolis mass flowmeters to measure its flow rate, enters a preheater to be heated to suitable temperature for experiments, then flows into the test section, and finally flows through a cooler after the test section and returns to the storage tank. In the bypass pathway, the CO_2 flows directly to the CO_2 storage tank after the pump, with its pressure regulated by a back-pressure valve, which helps to precisely adjust the flow rate in the main flow. The coolant circulation loop uses ethylene glycol as the coolant, which has two main functions: to

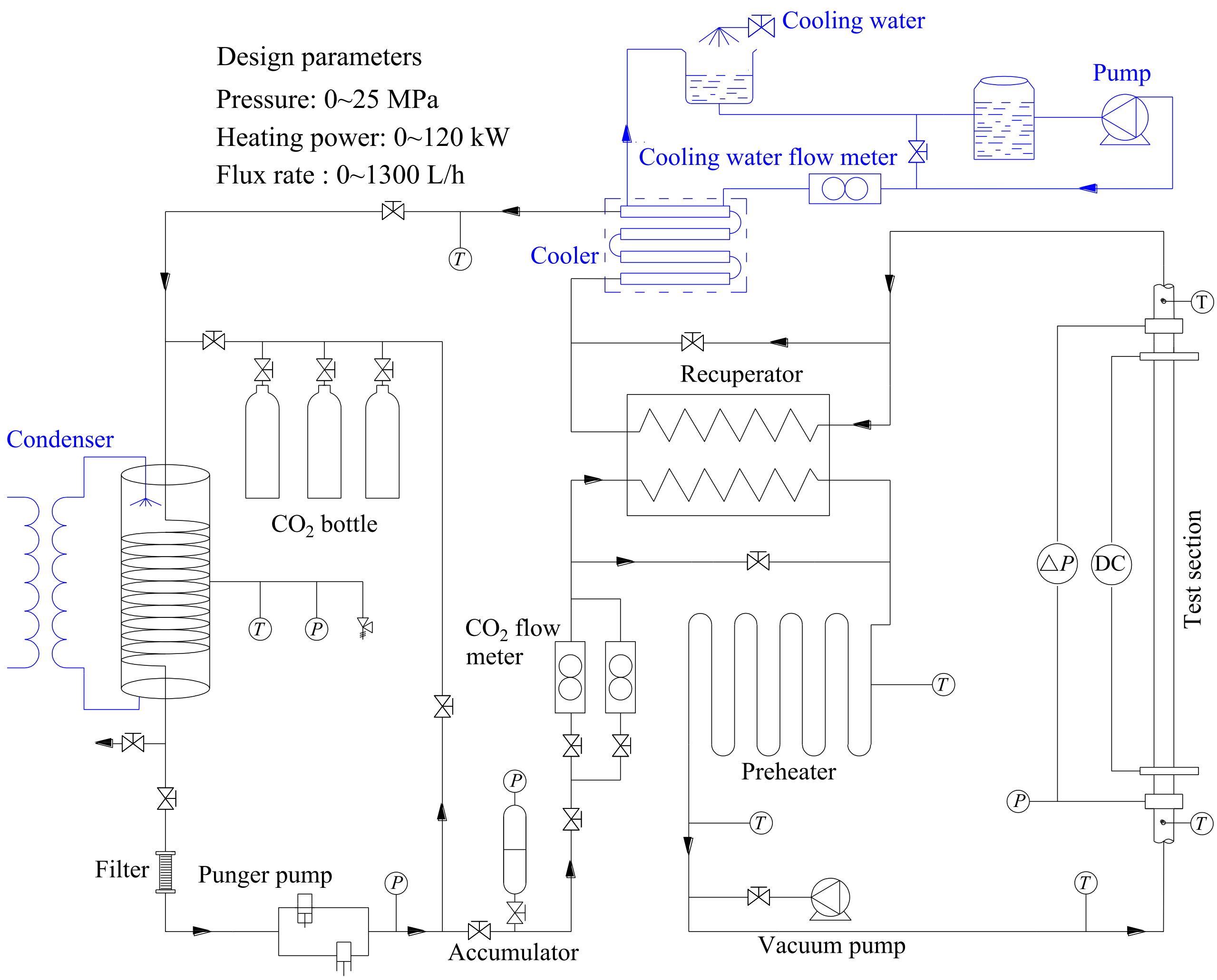

Fig. 1. Schematic of the experimental system. Reproduced with permission from Ref. [37]. Copyright 2020, Elsevier.

cool down the temperature of the CO_2 flow after the test section before it returns to the CO_2 storage tank, and to keep the CO_2 storage tank at low temperature, thereby keep the CO_2 in the storage tank in liquid state and ensure normal operation of the pump. Heat flux is supplied to the test tube by supplying direct current (DC) voltage to the tube material to generate joule heating. The heating power can be easily adjusted by varying the supplied voltage, with a maximum heating power of 120 kW.

In this work, three different test tubes are used. As shown in Fig. 2, the test tubes are all made of 1Cr18Ni9Ti stainless steel and have a total length of 3600 mm and an effective heating length of 2000 mm. The two 800 mm-long sections, one before and one after the heating section, are used to stabilize the flow. The tubes have inner diameters of 8, 10, and 12 mm, respectively, while the thickness of the tube wall is 2 mm for all three tubes. The tubes are arranged vertically in the experiments, with CO_2 flowing upward inside the tubes. Heating voltage is applied across the two copper electrodes welded onto the tube at both ends of the heating section. Temperatures of the tube outer wall are measured by K-type thermocouples positioned at 39 equally spaced cross sections (50 mm apart) along the heating section, which are directly welded onto the tube wall to eliminate thermal contact resistance. The inlet and outlet bulk fluid temperatures are measured using two sheathed thermocouples inserted into the center of the tube. The entire test section is also wrapped with 50 mm thick of thermal insulation material with a room temperature thermal conductivity of 0.035 W/m K to reduce heat loss to the ambient.

2.2. Data reduction

During experiments, the measured values include inlet pressure P_{in}, pressure drop ΔP, inlet fluid temperature $T_{b,in}$, outlet fluid temperature $T_{b,out}$, tube outer wall temperatures $T_{w,o}$, and CO_2 flow rate m. The data reduction process based on these measured values is shown below.

The mass flux G is calculated as

$$G = \frac{m}{\frac{1}{4}\pi d_i^2} \tag{1}$$

where d_i is the inner diameter of the test tube. The heating power P_c is calculated as

$$P_c = m\left(i_{b,out} - i_{b,in}\right) \tag{2}$$

where $i_{b,out}$ and $i_{b,in}$ are the fluid enthalpies at the outlet and the inlet, respectively, which are obtained from the NIST REFPROP software using the measured outlet and inlet temperatures, $T_{b,out}$ and $T_{b,in}$. The heat flux based on the inner tube wall surface area can be calculated as

$$q_w = \frac{P_c}{\pi d_i L} \tag{3}$$

where L is the effective heating length (L = 2000 mm). The heat transfer coefficient h along the axial flow length is calculated based on

$$h = q_w/(T_{w,i} - T_b) \tag{4}$$

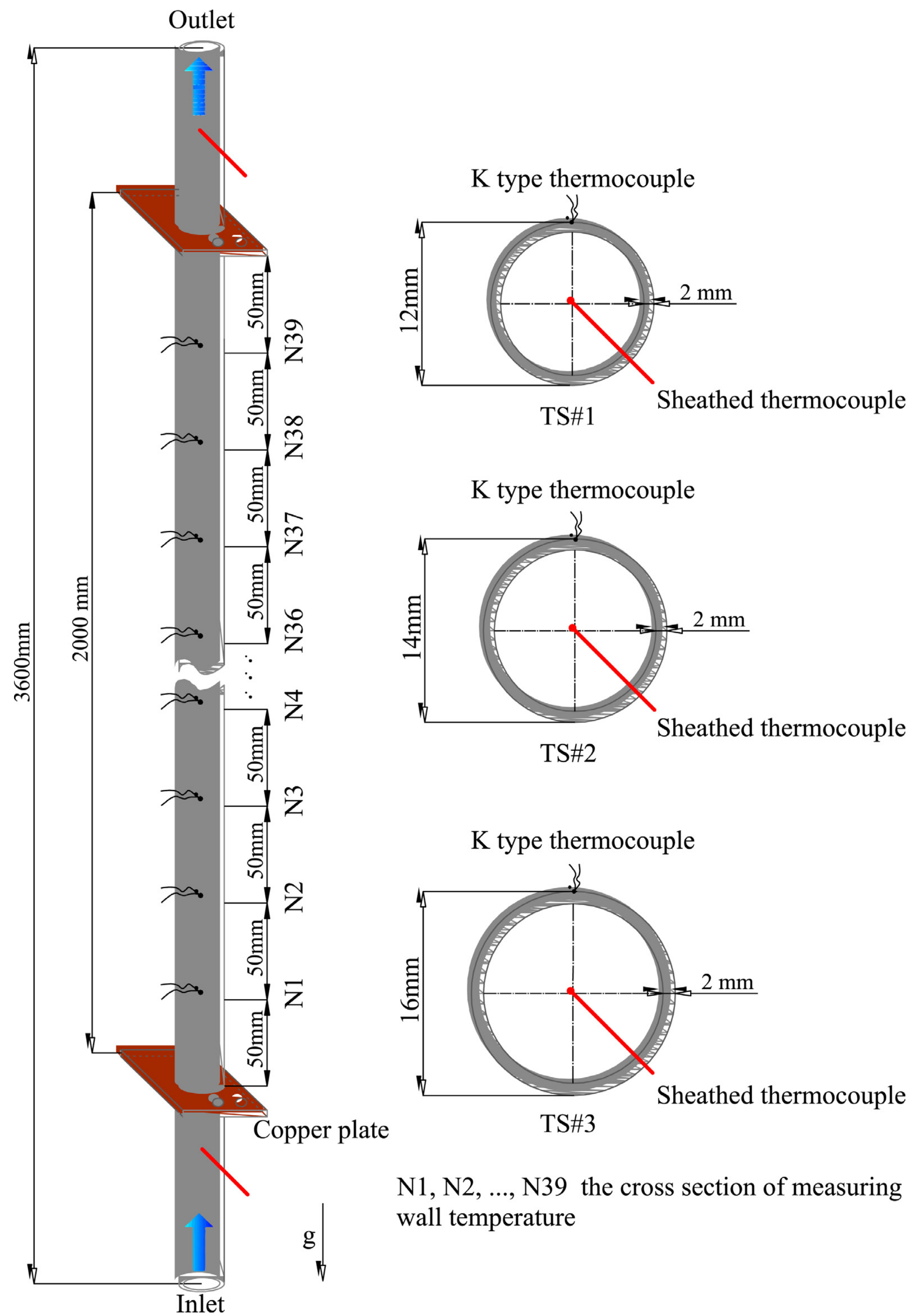

Fig. 2. The test tubes used in this work.

where $T_{w,i}$ is the inner wall temperature and T_b is the bulk fluid temperature, both of which changes along the axial flow length. Since the heating power is uniformly applied on the tube wall through joule heating, the inner wall temperature $T_{w,i}$ can be obtained using the one-dimensional heat conduction equation:

$$\frac{1}{r}\frac{d}{dr}\left(r\lambda\frac{dT}{dr}\right)+q=0 \tag{5}$$

where λ is the thermal conductivity of the stainless steel tube, r is the radial coordinate, and q is the volumetric heat generation rate represented by

$$q=\frac{P_c}{\frac{1}{4}\pi\left({d_o}^2-{d_i}^2\right)L} \tag{6}$$

where d_o and d_i are the outer and inner diameters of the tube. Eq. (5) has the following boundary conditions:

$$\left.\frac{dT}{dr}\right|_{r=r_o}=0 \tag{7}$$

$$T|_{r=r_o}=T_{w,o} \tag{8}$$

where r_o is the outer radius of the tube.

Solve Eq. (5) using boundary conditions Eqs. (7)-(8) for T and set $r = r_i$ where r_i is the inner radius of the tube, the inner wall temperature can be obtained as

$$T_{w,i}=T_{w,o}-\frac{q_w d_i}{2\lambda}\left(\frac{1}{2}-\frac{d_i^{\,2}}{d_o^{\,2}-d_i^{\,2}}\ln\frac{d_o}{d_i}\right) \tag{9}$$

The bulk fluid temperature T_b changes from $T_{b,in}$ to $T_{b,out}$ along the heating section. The local T_b can be obtained based on the local pressure P and the local bulk fluid enthalpy i_b. The local pressure P used to evaluate the fluid enthalpy is assumed to be equal to the inlet pressure P_{in}, based on the fact that the pressure drop across the test tube during experiments is several orders of magnitude smaller than the inlet pressure P_{in}. The local bulk fluid enthalpy i_b is obtained using energy conservation as

$$i_b=i_{b,in}+\frac{q_w\pi d_i z}{m} \tag{10}$$

where z is the axial coordinate starting from the bottom of the heating section.

The measured total pressure drop ΔP across the heating section includes three components:

$$\Delta P=\Delta P_f+\Delta P_g+\Delta P_{ac} \tag{11}$$

where the subscripts f, g, and ac represent the pressure drops from friction, gravity, and acceleration, respectively. The gravitational pressure drop for the vertical upward flow is calculated as

$$\Delta P_g=\left(\frac{T_{b,in}\rho_{in}-T_{b,out}\rho_{out}}{T_{b,in}+T_{b,out}}\right)gL \tag{12}$$

where g is the gravitational acceleration, ρ is the bulk fluid density, and the subscripts out and in represent outlet and inlet conditions, respectively.

The pressure drop from acceleration can be calculated as

$$\Delta P_{ac}=\rho_{out}u_{out}^{\,2}-\rho_{in}u_{in}^{\,2}=G^2\left(\frac{1}{\rho_{out}}-\frac{1}{\rho_{in}}\right) \tag{13}$$

where u is the mean fluid velocity.

The frictional pressure drop can then be obtained as

$$\Delta P_f=\Delta P-\Delta P_g-\Delta P_{ac} \tag{14}$$

Finally, the friction coefficient f is defined by

$$f=\Delta P_f\frac{d_i}{L}\frac{G^2}{2\rho_{ave}} \tag{15}$$

where ρ_{ave} is the average fluid density evaluated at the average temperature along the tube, $T_{ave} = (T_{b,in}+T_{b,out})/2$. It is worth noting that the pressure drop is negligibly small compared to the fluid pressure and thus has negligible effect on the heat transfer. For example, during experiment with pressure of 15.545 MPa, mass flux of 1000 kg/m^{2}s, heat flux of 120.32 kW/m^2, and tube diameter of 8 mm, the measured pressure drop along the tube length is 25.354 kPa, which is only 0.16% of the working pressure.

2.3. Uncertainty analysis

The apparatuses and devices used in the experiments were carefully calibrated prior to the experiments to ensure accuracy of the measurements. The mass flow rate is measured using a Coriolis mass flowmeter (DMF-1-3-B, accuracy 0.2%) and is calibrated before the experiments, showing an uncertainty of 2.05%. Inlet and outlet fluid temperatures are measured using ϕ3 mm sheathed K-type thermocouples, and the tube outer wall temperatures are measured using ϕ0.25 mm K-type thermocouples (Omega NiCr-NiSi), both with an uncertainty of 0.5 °C. The operation pressure of the system is measured using a Rosemount 3051 pressure transducer with an uncertainty of 1%. Due to the wide range of pressure drop in the experiments, the pressure drop across the test section is measured using two Rosemount 1151 differential pressure transducers with different measurement ranges, with an uncertainty of 2.06%. The DC voltage applied on the test tube is monitored by a S4-DT DC voltage transducer as DC voltage signal in the range of 0~5 V, which has an accuracy of 0.2%. The data acquisition system uses an ADAM-4118/4117 module which has an accuracy of 0.2%.

For a parameter R that is not directly measured but can be calculated using directly measured quantities (x_1, x_2, ..., x_N), i.e., $R = f(x_1, x_2, \cdots, x_N)$, the uncertainty of R can be represented using error propagation equation

$$\Delta R=\sqrt{\left(\frac{\partial R}{\partial x_1}\delta x_1\right)^2+\left(\frac{\partial R}{\partial x_2}\delta x_2\right)^2+\cdots+\left(\frac{\partial R}{\partial x_N}\delta x_N\right)^2} \tag{16}$$

where δx_1, δx_2, $\cdots$, δx_N are the uncertainties of x_1, x_2, ..., x_N, respectively. Using this equation, the calculated uncertainties for the wall heat flux q_w, the inner wall temperature $T_{w,i}$, the heat transfer coefficient h, and the friction coefficient f are 5.05%, 0.5%, 8.64%, and 3%, respectively.

2.4. Experimental system validation

Although the test section is wrapped with thick thermal insulation, the tube wall temperature during experiments can be significantly higher than the environment, resulting in non-negligible heat loss to the environment. The thermal efficiency η_{th} is defined as the ratio of the actual heating power to the test section P_c to the total electric heating power P_e:

$$\eta_{th}=\frac{P_c}{P_e}=\frac{m\left(i_{b,out}-i_{b,in}\right)}{UI} \tag{17}$$

where U and I are the heating voltage and current, respectively. The thermal efficiency is calculated for various experimental working conditions as shown in Fig. 3a. The thermal efficiency is above 90% for most of the experiments except for the cases when the outlet fluid temperature $T_{b,out}$ is close to the pseudocritical temperature T_{pc}. This is because the specific heat capacity of the fluid reaches maximum at T_{pc}, and consequently, given certain heating power, the temperature rise can be very small, resulting in large uncertainty due to error in the temperature measurement.

The experimental system was also validated by a set of repeating experiments, as shown in Fig. 3b-c. With the same operating conditions for experiments performed on different days, the experimental results were almost identical for both NHT and HTD cases, demonstrating validity of the system and repeatability of the experiments.

3. Results and discussions

In this work, the pressure P, the mass flux G, and the heat flux applied on the wall q_w covered the ranges of 7.5~23 MPa,

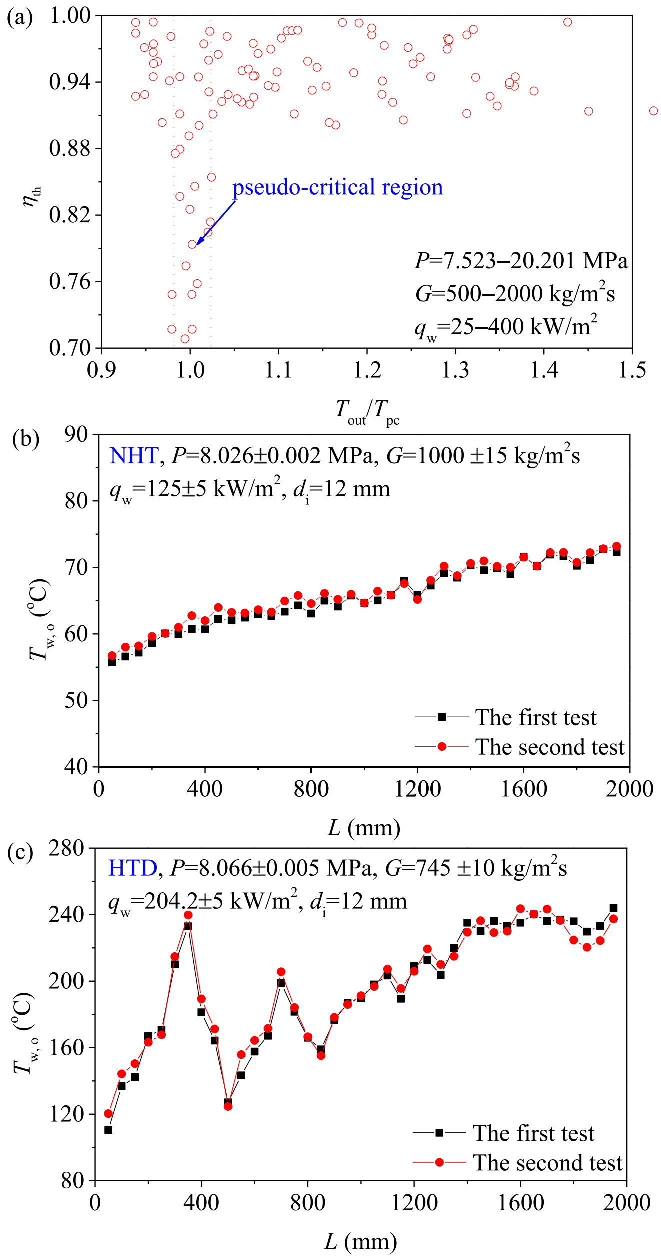

Fig. 3. Calibration of the experimental system. (a) Thermal efficiency of the system under various working conditions. (b) Repeatability test for normal heat transfer (NHT) mode. (c) Repeatability test for heat transfer deterioration (HTD) mode.

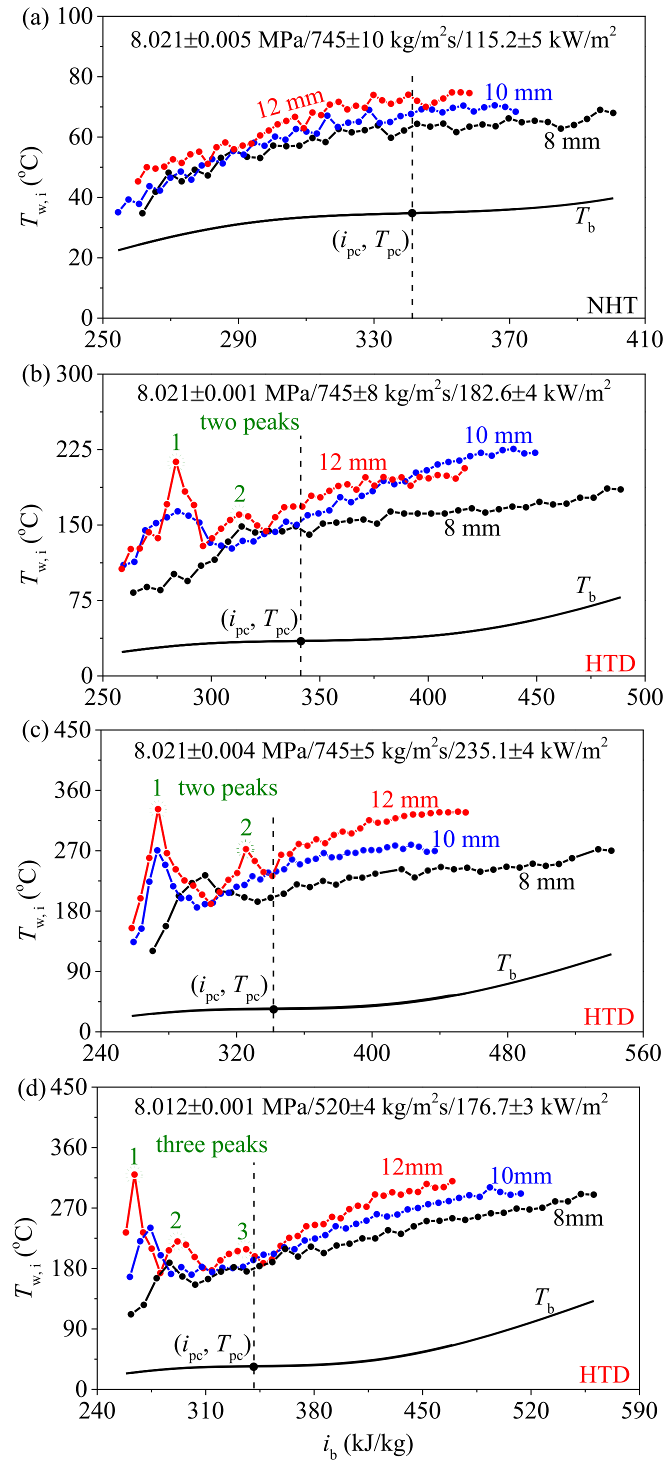

Fig. 4. Effect of tube diameter on inner wall temperatures under low pressures.

400~1500 kg/m^{2}s, and 25~450 kW/m^2, respectively. The inner diameter of the test tubes was varied for three values: 8 mm, 10 mm, and 12 mm.

3.1. Effect of tube diameter on the inner wall temperature distribution

Figs. 4-5 shows the heat transfer performance for various working conditions, with each panel in these figures representing one combination of $P/G/q_w$. The curves are shown as the inner wall temperature $T_{w,i}$ versus the bulk fluid enthalpy i_b. The bulk fluid temperature T_b as a function of i_b, and the temperature and enthalpy at the pseudocritical point, i_{pc} and T_{pc}, are also shown in each panel under corresponding experimental conditions. In this work, the HTD mode is defined according to the Type 1 HTD based on T_w peak [42]. We define the formation of a temperature peak based on the following criterion: when $T_b<T_{pc}<T_{w,i}$ is satisfied, a temperature peak is counted when the temperature rise ΔT (as shown in Fig. 7c) exceeds 8 °C, to avoid the error caused by measurement uncertainty of the thermocouples. This definition is the same one used in Ref. [33]. Besides, in this work, we only conducted experiments with upward flow conditions. Therefore, although the flow direction is expected to affect our experimental results, this effect of gravitational force is not considered in this work. Nevertheless, we expect since different flow directions will

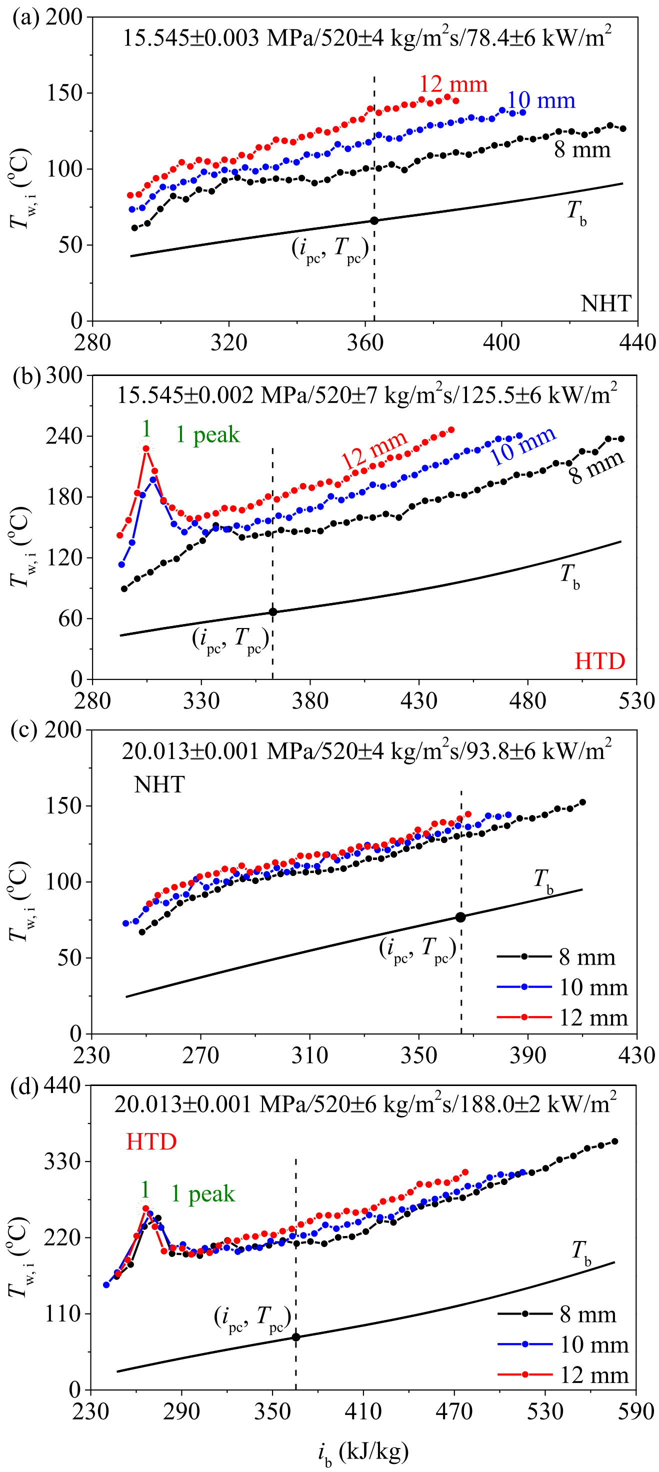

Fig. 5. Effect of tube diameter on inner wall temperatures under high pressures.

influence the velocity distribution, which requires further study in the future.

Fig. 4 shows the inner wall temperature distribution curves under ~8 MPa pressure for three different tube diameters. Generally, with the same pressure, mass flux, and wall heat flux, the wall temperature increases with increasing tube diameter. With mass flux G of 745 kg/m^{2}s and wall heat flux q_w of 115.2 kW/m^2, the wall temperature profiles for test tubes with 8, 10, and 12 mm inner diameters all display relatively smooth increase over the bulk fluid enthalpy, as shown in Fig. 4a, indicating NHT mode. With increasing tube diameter from 8 to 12 mm, the wall temperature at the same bulk fluid enthalpy increases. When the heat flux is increased to 182.6 kW/m^2, as shown in Fig. 4b, instead of rising gradually and smoothly, the wall temperature for all three diameters shows at least one sudden increase and then return to normal afterwards, forming peaks in the wall temperature curves, which indicates HTD mode. For 8 mm and 10 mm tubes, only one temperature peak exists before the bulk fluid enthalpy reaches the pseudocritical enthalpy. For 12 mm tube, two temperature peaks are observed: the first one closer to tube entrance is taller and narrower, while the second one is shorter and wider, and both appear before the bulk fluid reaches the pseudocritical point. A valley is formed in between the two consecutive peaks, which corresponds to the recovery to normal wall temperature after the first temperature peak. For practical application, when a wall temperature peak is formed, it might cause significant safety issue due to overheating, while a wall temperature valley does not induce any heat transfer anomaly. Thus, the peaks are of greater interest compared to the minimum values, and in this work, we only focus on the temperature peaks. When the heat flux is further increased to 235.1 kW/m^2, as shown in Fig. 4c, the two peaks for 12 mm curve and the single peak in 10 mm and 8 mm curves are more significant compared to the corresponding peaks in Fig. 4b, demonstrating further deteriorated heat transfer with increasing heat flux. Fig. 4d shows the temperature profiles for G of 520.4 kg/m^{2}s and q_w of 176.7 kW/m^2. The heat flux is close to the heat flux of 182.6 kW/m^2 shown in Fig. 4b. However, the smaller mass flux results in three peaks in the curve for the 12 mm tube, while the curves for the 8 mm and 10 mm tubes still show only one peak.

Fig. 5 shows the inner wall temperature distribution curves under ~15.5 MPa and ~20 MPa pressures for three different tube diameters. At ~15.5 MPa, when the wall heat flux is small (78.4 kW/m^2), the wall temperature rises gradually with the bulk fluid enthalpy and there is no HTD observed for all three tubes, as shown in Fig. 5a. For the same bulk fluid enthalpy, the wall temperature is generally higher for larger tube diameter, which is similar to the trend observed for ~8 MPa experimental condition in Fig. 4 described above. When the heat flux is increased to 125.5 kW/m^2, HTD occurrs for all three tubes, as shown in Fig. 5b, but with only one temperature peak for each curve. The curve for 8 mm tube shows the smallest temperature peak, while the curve for 12 mm tube has a more abrupt temperature peak. When the working pressure is raised to ~20 MPa, at a small heat flux of 93.8 kW/m^2, all three tubes show NHT mode, with very small difference in their wall temperature profiles, as shown in Fig. 5c. When the heat flux is increased to 188 kW/m^2, all three tubes show HTD mode with only one temperature peak, as shown in Fig. 5d. The difference between the curves is also small, similar to Fig. 5c with low heat flux. Notably, for the HTD cases shown here, the temperature peaks appear at the front of the tube. This is because when the fluid temperature is below the pseudocritical temperature T_{pc}, the specific heat is generally small. Therefore, under high heat fluxes, the bulk fluid temperature T_b along the tube quickly increases and approaches T_{pc} within a short length. Since the occurrence of HTD requires $T_b<T_{pc}$ (which will be discussed in later sections), the HTD peaks form in the front of the tube.

From the observations described above, it can be seen that the heat transfer characteristics are affected by the tube diameter. Under NHT conditions, with the same bulk fluid enthalpy, the increase of tube diameter results in the increase of wall temperature, indicating a decrease of heat transfer coefficient, as shown in Fig. 4a, 5a, and 5c. This effect of tube diameter on the heat transfer characteristics diminishes with increasing working pressure. Under HTD conditions, at ~8 MPa and ~15.5 MPa, smaller tube diameter causes increased HTC and reduces the magnitude of the deteriora-

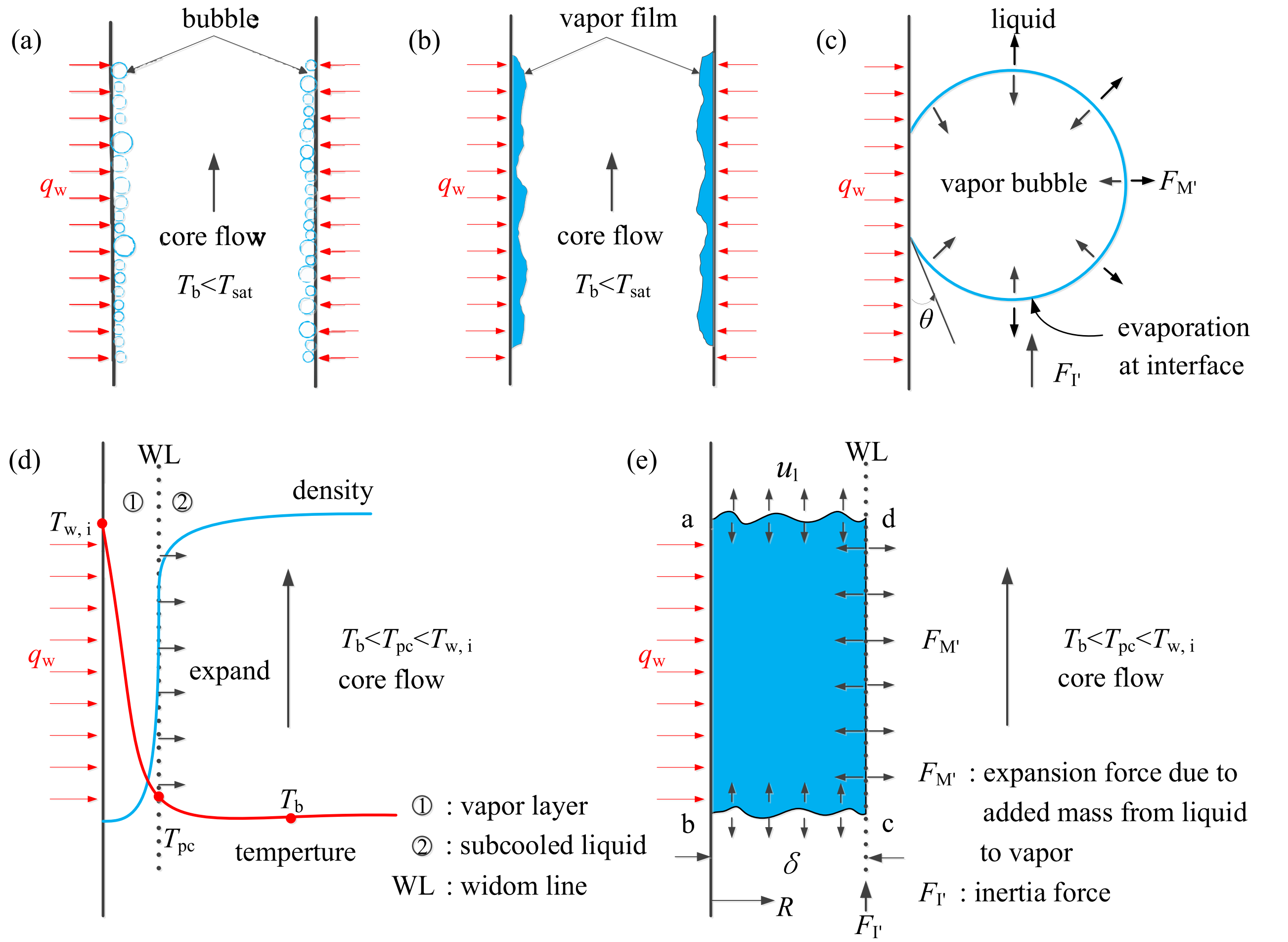

Fig. 6. Schematics showing the analogy between subcritical boiling and supercritical pseudo-boiling. (a) Subcritical nucleate boiling; (b) subcritical film boiling; (c) evaporation momentum force and inertia force on the bubble; (d) supercritical pseudo-boiling; (f) evaporation momentum force and inertia force on the "vapor film".

tion peak as shown in Fig. 4b-d and Fig. 5b, which agrees with conclusion from Shiralkar and Griffith [19]. However, when the pressure is raised to ~20 MPa, the effect of tube diameter on the heat transfer characteristics also diminishes as shown in Fig. 5d, similar to the NHT cases. In general, with the same working conditions, larger tube diameter causes larger wall temperature, and consequently smaller HTC, and the effect is weaker at higher pressure. The reason for the decreased HTC with increased tube diameter is that with the same working conditions, larger tube diameter causes smaller velocity gradient near the tube wall and consequently smaller shear stress and smaller local inertia force acting on the "vapor film", resulting in worse heat transfer. It is worth mentioning that larger tube diameter causing smaller local inertia force is not in conflict with the definition of Reynolds number *Re*. Although under the same working conditions, a larger tube diameter indicates a larger *Re*, it only means that the ratio of the inertia force to the viscous force is larger, and does not necessarily mean a larger inertia force.

3.2. Transition boundary between NHT and HTD

Although different tube diameters result in different heat transfer characteristics, among the three tubes studied in this work, the tube diameter does not affect whether HTD occurs or not: for a given combination of *P*, *G*, q_w, either all three tubes show NHT, or all of them show HTD, as shown in Figs. 4-5. The reason can be understood by the pseudo-boiling concept as discussed below.

At subcritical pressures, when subcooled fluid with bulk temperature T_b flows along a circular tube with a heat flux q_w applied on the tube wall, the nucleate boiling regime (Fig. 6a) has enhanced heat transfer, while the film boiling regime (Fig. 6b) has deteriorated heat transfer. The transition between nucleate boiling and film boiling for subcritical flow inside tubes is essentially governed by the competition between the following two forces: the evaporation momentum force which tends to adhere the bubble on the wall, and the inertia force which tends to detach the bubble from the wall [43], as shown in Fig. 6c.

The evaporation momentum force acting on the bubble interface can be represented by [44]

$$F_{M'} = \left(\frac{q_w}{i_{fg}}\right)^2 \frac{1}{\rho_v} \tag{18}$$

where q_w is the heat flux, i_{fg} is the latent heat of vaporization, and ρ_v is the vapor density. On the other hand, the inertia force imposed on the bubble, generated by the convective flow in the tube, can be expressed as [44]

$$F_{I'} = \frac{G^2}{\rho_l} \tag{19}$$

where *G* is the mass flux and ρ_l is the liquid density. The K_1 number, defined as the ratio of the evaporation momentum force to the inertia force, reflects the relative importance of the two forces

[44]

$$K_1 = \frac{F_{M'}}{F_{I'}} = \left(\frac{q_w}{Gi_{fg}}\right)^2 \frac{\rho_l}{\rho_v} = Bo^2 \frac{\rho_l}{\rho_v} \tag{20}$$

Where Bo is the boiling number, $Bo = q_w/Gi_{fg}$.

At supercritical pressures, when the pseudocritical temperature T_{pc} is in between the tube inner wall temperature $T_{w,i}$ and the bulk fluid temperature T_b, i.e., $T_{w,i} > T_{pc} > T_b$, "two-phase" can also exist in the tube, with the WL being the boundary between liquid-like and gas-like phases, as shown in Fig. 6d. Due to the significant variation of thermophysical properties when crossing the WL, an analogy between supercritical heat transfer and subcritical boiling can be performed. Hence, there are also two competing forces: the evaporation momentum force to press the "vapor film" against the wall, and the inertia force to detach the "vapor film" from the wall. In analogous to subcritical boiling, dimensionless numbers for subcritical boiling described above have also been applied for supercritical heat transfer and represent the competition between evaporation momentum force and inertia force as shown in Fig. 6e, but with modified formulas. The supercritical boiling number, *SBO*, is defined as

$$SBO = \frac{q_w}{Gi_{pc}} \tag{21}$$

where i_{pc} is the enthalpy at the pseudocritical point. The latent heat in the subcritical boiling number is replaced by i_{pc} in the *SBO*, due to the complexity in defining and calculating pseudo-phase-change enthalpy at supercritical pressures. The *K* number for supercritical heat transfer is represented by

$$K = SBO^2 \frac{\rho_b}{\rho_w} \tag{22}$$

where ρ_b and ρ_w are the fluid density at T_b and $T_{w,i}$, respectively.

SBO represents the relative dominance of the global evaporation momentum force and inertia force. A large *SBO* indicates dominance of the global evaporation momentum force, and a small *SBO* indicates dominance of the global inertia force. In Refs. [33,34], pseudo-boiling has been demonstrated to well-capture the experimental trend, with the supercritical boiling number *SBO* being the criterion to distinguish NHT and HTD: when *SBO* is smaller than certain critical value, the heat transfer is in the NHT mode; when *SBO* is larger than the critical value, the heat transfer is in the HTD mode. The critical *SBO* identified in Ref. [33] for supercritical CO_2 with 10 mm diameter tube was $SBO_{cr} = 5.126\times10^{-4}$. In this work, analyzing the experimental results for 8, 10, and 12 mm tubes, it is found that the tube diameter has no obvious effect on the critical *SBO*: the critical *SBO* for three different tube diameters ranges from $4.978\text{~}5.204\times10^{-4}$, which is within 3% from the SBO_{cr} identified before. As shown in Fig. 7, when the *SBO* is slightly smaller than SBO_{cr}, the heat transfer mode is NHT (Fig. 7a), but when the *SBO* is slightly larger than SBO_{cr}, the heat transfer mode transitions to HTD (Fig. 7b).

Fig. 8 shows the comparison of our experimental results with two existing criteria for HTD occurrence shown in Table 1, one buoyancy criterion and one acceleration criterion. As shown in Fig. 8, both of these criteria cannot accurate predict HTD occurrence, which is consistent with Refs. [15,17]. On the other hand, *SBO* is shown to be a useful criterion. Fig. 9 shows the wall heat flux q_w and the wall temperature rise ΔT with varying *SBO*. The 8 mm, 10 mm, and 12 mm data points are our experimental results, while the 2 mm data points are obtained from Ref. [45]. In Fig. 9, black points represent NHT while red points represent HTD. It is clearly shown in Fig. 9a that the occurrence of HTD does not depend on q_w alone: given a certain q_w, both NHT and HTD can happen. However, using *SBO* as the criterion, experimental results for different tube diameters can be well distinguished. In

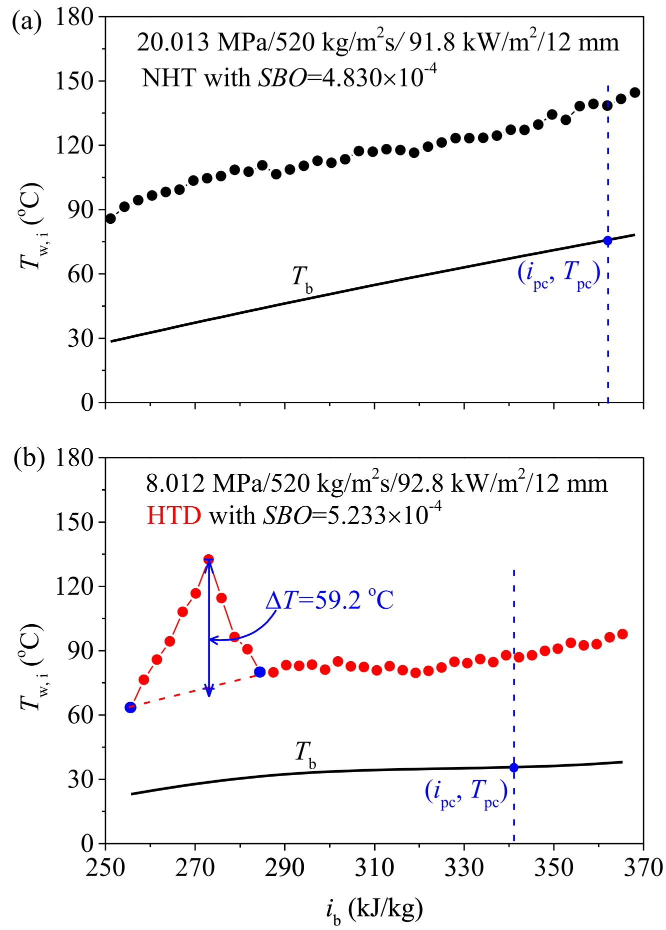

Fig. 7. Sudden changes between two heat transfer modes with small deviation from the critical *SBO*. (a) Normal heat transfer (NHT) mode, i_{pc} = 365.44 kJ/kg, T_{pc} = 75.9 °C; (b) heat transfer deterioration (HTD) mode, i_{pc} = 341.4 kJ/kg, T_{pc} = 34.7 °C.

Fig. 9b, it can also be clearly seen that when $SBO<SBO_{cr}$, the wall temperature rise is very small, corresponding to NHT regime, but when $SBO>SBO_{cr}$, the temperature rise becomes significant, indicating HTD regime. In our experiments, the maximum temperature rise was as high as ~185 °C. It is worth noting that although the equation for *SBO* does not contain pressure *P*, the effect of pressure is incorporated in *SBO*, since the pseudocritical enthalpy i_{pc} is dependent on *P*.

As discussed previously, the equation for *SBO* contains the following three parameters: the wall heat flux q_w, the mass flux *G*, and the pseudocritical enthalpy i_{pc}, as shown in Eq. (21). Hence, the concept of using *SBO* as the critical parameter to distinguish NHT and HTD inherently assumes that the HTD occurrence should be independent of the tube diameter, which is exactly what has been observed in this work. Therefore, the pseudo-boiling concept agrees well with the experimental results. As will be discussed later, the *SBO* is a global parameter which can be used for judging the onset of HTD but does not describe the detailed heat transfer feature along the tube.

3.3. Multi-peak phenomenon in HTD regime

In Section 3.1, the wall temperature profiles for different tube diameters under various working conditions was discussed. It is found that when the heat transfer mode is HTD, multi-peak phenomenon can occur. Fig. 10 shows the wall temperature and the heat transfer coefficient as functions of the bulk fluid enthalpy for

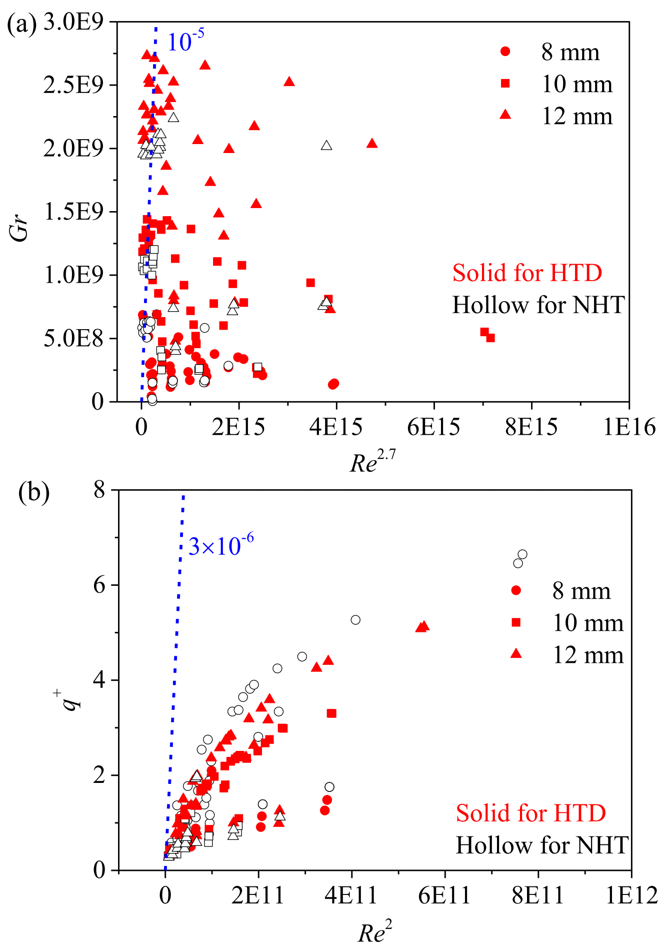

Fig. 8. Comparison between the experimental results of this work to existing criteria. (a) The buoyancy criterion by Jackson et al. [20] (b) The acceleration criteria by McEligot et al. [24]

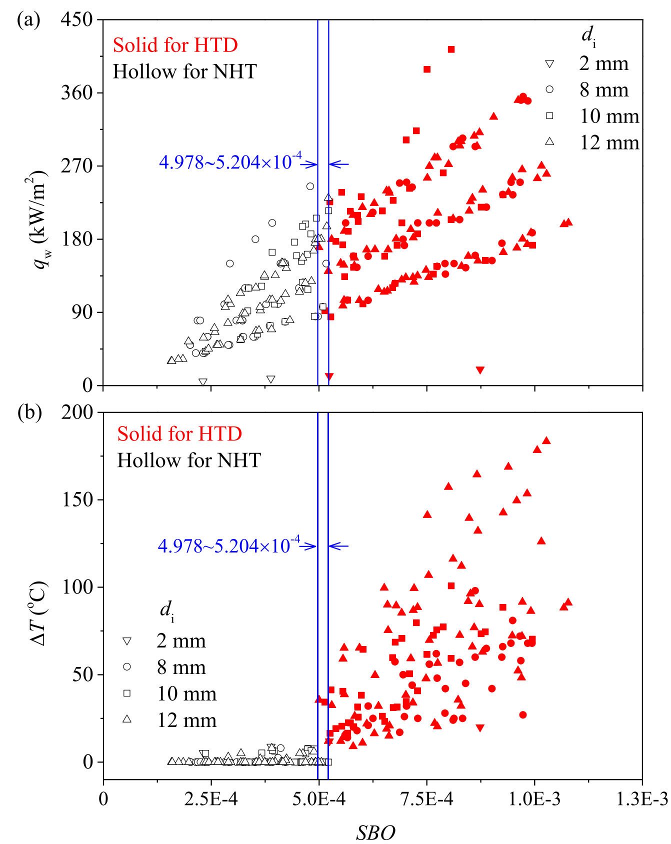

Fig. 9. Wall heat flux q_w (a) and temperature rise ΔT (b) versus *SBO* for different tube diameters. (hollow black symbols for NHT and solid red symbols for HTD. The 2 mm data were obtained from Ref. [45])

the four types of heat transfer mode observed in this study, including one NHT mode and three different HTD modes. Fig. 10a shows the typical NHT mode, having a smooth temperature profile and correspondingly a smooth HTC curve, which usually occurs with small heat flux and large mass flux. Fig. 10b, c, and d show the HTD mode with a single temperature peak, two temperature peaks, and three temperature peaks, respectively. The one, two, and three peaks in the temperature profiles also correspond to one, two, and three valleys in the HTC curves, respectively.

Fig. 11 plots the heat flux q_w vs. the mass flux G for 10 mm (a-b) and 12 mm (c-f) tubes under various pressures. The green dashed line represents the transition boundary between NHT and HTD modes, the blue dashed line represents the boundary between $n = 1$ and $n = 2$, and the red dashed line represents the boundary between $n = 2$ and $n = 3$, where n is the number of peaks observed in the temperature distribution profiles. For 10 mm tube at both low pressure (~8 MPa) and high pressure (~15.5 MPa), only single peak mode is observed in HTD regime, as shown in Fig. 11 a-b. Same behavior is also observed in 8 mm tube and is thus not shown here. However, for 12 mm tube, multiple peaks appear in HTD regime. As shown in Fig. 11c, at low pressure of ~8 MPa, with the same mass flux, the increase of heat flux causes the transition from NHT to HTD with one peak initially, then with two peaks, and finally with three peaks. When the pressure is increased to ~12.5 MPa, the three-peak mode disappears, and only single-peak and two-peak modes are observed in HTD regime, as shown in Fig. 11d. At higher pressures of ~15.5 MPa and ~20 MPa, multi-peak phenomenon disappears, and only single-peak mode is present, as shown in Fig. 11 e-f. Hence, the multi-peak phenomenon tends to occur with larger tube diameter and lower pressure. Moreover, as shown in Fig. 11, with increasing mass flux, the heat flux required for HTD to occur is larger, which can be understood from Eq. (21) for *SBO*, the transition criterion between NHT and HTD. Increased mass flux results in increased inertia force, and consequently, increased evaporation momentum force induced by increased heat flux is needed to achieve HTD. Besides, increasing mass flux can also decrease the magnitude of the first peak and consequently decrease the number of peaks, as shown in Fig. 5 b and d, which is also due to the larger inertia force which suppress the thickening of the “vapor film”.

As mentioned before, similar multi-peak phenomenon was observed by Bourke et al. [38] in supercritical CO_2 flowing upward in a vertical tube with inner diameter of 22.8 mm. When heat flux exceeded certain value, two peaks formed in the wall temperature profile, with the first one taller and steeper than the second one. Jackson et al. [40] also observed multiple peaks in the wall temperature distribution of supercritical CO_2 flowing in a 19 mm diameter tube, and the peaking was more pronounced with increasing heat flux. However, both authors did not conduct further experiments to study this phenomenon and its reasons and underlying mechanisms. It is worth mentioning that in our previous work, using *SBO* as the criterion for transition between NHT and HTD has been shown to be valid for four different supercritical fluids (CO_2, water, R22, R134a) with wide parameter ranges, including tube diameters. Our conclusion can also be applied to Bourke et al. [38] with 22.8 mm tube quite well, but it has certain variation when describing the experimental results of Jackson et al. [40] with 19 mm tube, which requires further experimental investigation with large tube diameter and wide parameter ranges.

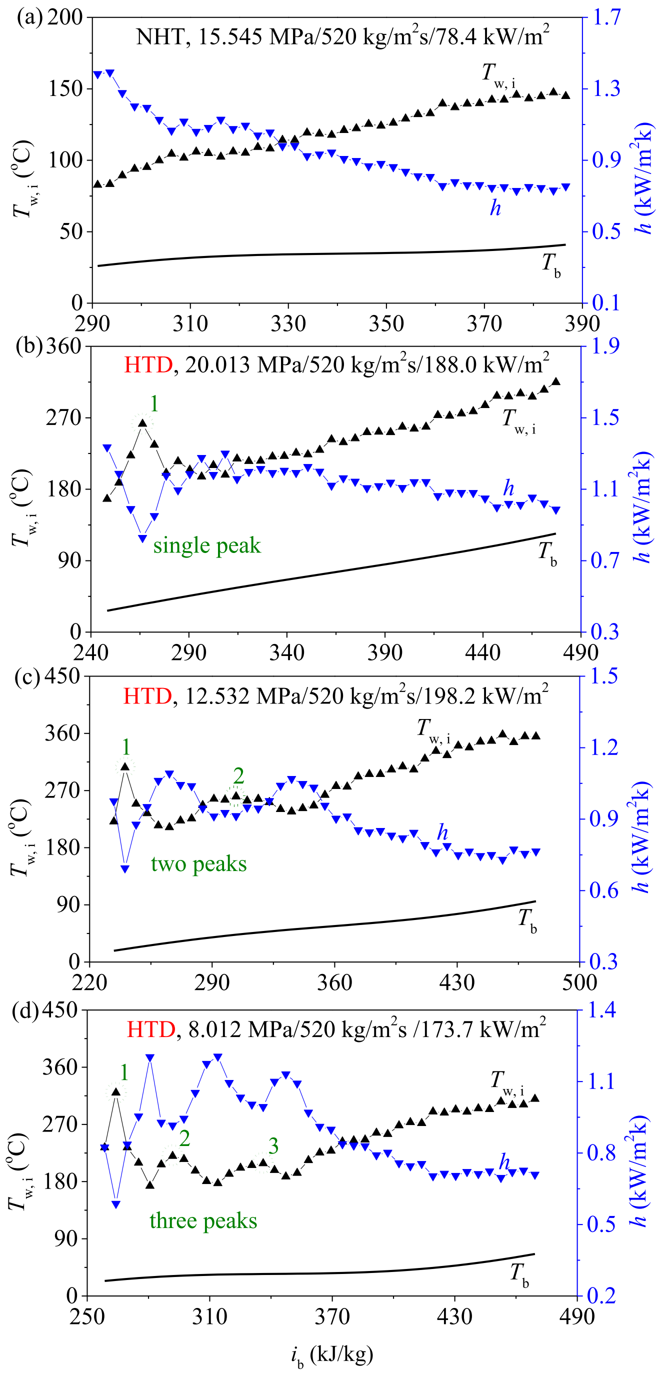

Fig. 10. Four types of heat transfer modes observed in the experiments (d_i = 12 mm).

Our experimental results show that for the three tubes studied in this work, varying the diameter of the test tube does not alter the onset of HTD, but affects the deterioration mode and magnitude. With a larger diameter, the temperature rise is larger when HTD occurs. This is because with constant mass flux and pressure, larger tube diameter results in a smaller velocity gradient near the tube wall, which causes a smaller inertia force on the “vapor film”. Hence, a larger tube diameter renders a thicker “vapor film” under the same working condition, causing worse heat transfer due to the low thermal conductivity of the gas-like phase, which induce a dominantly large thermal resistance. Moreover, multi-peak phenomenon is only observed in the 12 mm tube but not in the tubes with smaller diameters, which is due to the larger temperature rise for larger diameter as discussed below.

In Fig. 12, the experimental data points shown in Fig. 9b are plotted again with different colors representing different HTD modes. Fig. 12 serves as a pattern map to distinguish different modes. The left of the graph represents the NHT mode, which has very small temperature rise. The lower-right corner represents the HTD mode with single temperature peak, while the upper-right corner represents the HTD mode with multiple peaks. Fig. 12 shows that in the HTD regime, whether multi-peak phenomenon occurs or not is not dependent on the *SBO*. Instead, it is highly dependent on the temperature rise: multi-peak cases have significantly larger temperature rise than single-peak cases. Hence, larger diameter results in larger temperature rise, which then causes the formation of multiple peaks.

The experimental results also show that the multi-peak phenomenon only occurs at low pressures. This is because with increasing pressure, the expansion coefficient of the fluid decreases, and it is more difficult for the “vapor film” to expand. Thus, the “vapor film” in the near wall region is thinner for larger pressure. Similar to the effect of decreasing the tube diameter, increasing the pressure results in thinner “vapor film” and consequently smaller temperature rise, which causes the disappearance of the multi-peak phenomenon.

3.4. Mechanism of the multi-peak phenomenon: orifice contraction effect

In this section, the reason for the occurrence of multi-peak phenomenon is discussed based on the pseudo-boiling concept. As discussed before, *SBO* represents the competition between the evaporation momentum force and the inertia force. When the *SBO* exceeds the critical *SBO*, the evaporation momentum force dominates, and the “vapor film” starts to thicken consequently. The thick “vapor film” induces large thermal resistance due to the low thermal conductivity of the gas-like phase, and causes heat transfer deterioration and sharp rise of wall temperature, similar to film boiling at subcritical pressure. After the sharp rise, the wall temperature reduces to normal temperature, which indicates that the heat transfer is improved and the “vapor film” thickness of the gas-like phase is reduced. Hence, multiple temperature peaks in the wall temperature profile corresponds to multiple thickness peaks in the “vapor film” thickness, which indicates the formation of multiple “vapor” orifices to block fluid flow. Therefore, it is expected that multi-peak cases have larger friction factor than single-peak cases, since the flow is blocked multiple times.

Fig. 13 shows the friction factors f of the experiments versus the Reynolds number *Re*. The friction factor f is shown to be larger for the HTD mode than for the NHT mode, which has also been observed in Ref. [37]. More importantly, in the HTD regime, the multi-peak cases (red triangles and blue diamonds) have larger friction factors than single-peak cases (green squares). This is because the NHT cases have relatively smooth “vapor film” along the tube, which results in small friction factor; while the HTD cases have the “vapor” orifices formed in the tube wall, which contracts the fluid flow and results in larger friction factor. Moreover, the multi-peak cases encounter multiple orifices and multiple contraction events, while the single-peak cases only encounter one orifice and one contraction. Hence, multi-peak cases are accompanied by larger friction factors.

The reason for the formation of orifice can be explained based on the competition between the local evaporation momentum force and local inertia force. When HTD occurs, the near wall region is occupied by “vapor film”, while the tube core is occupied by liquid-like fluid. Fig. 14a shows the wall temperature profile for a typical single peak case, and the temperature peak corresponds

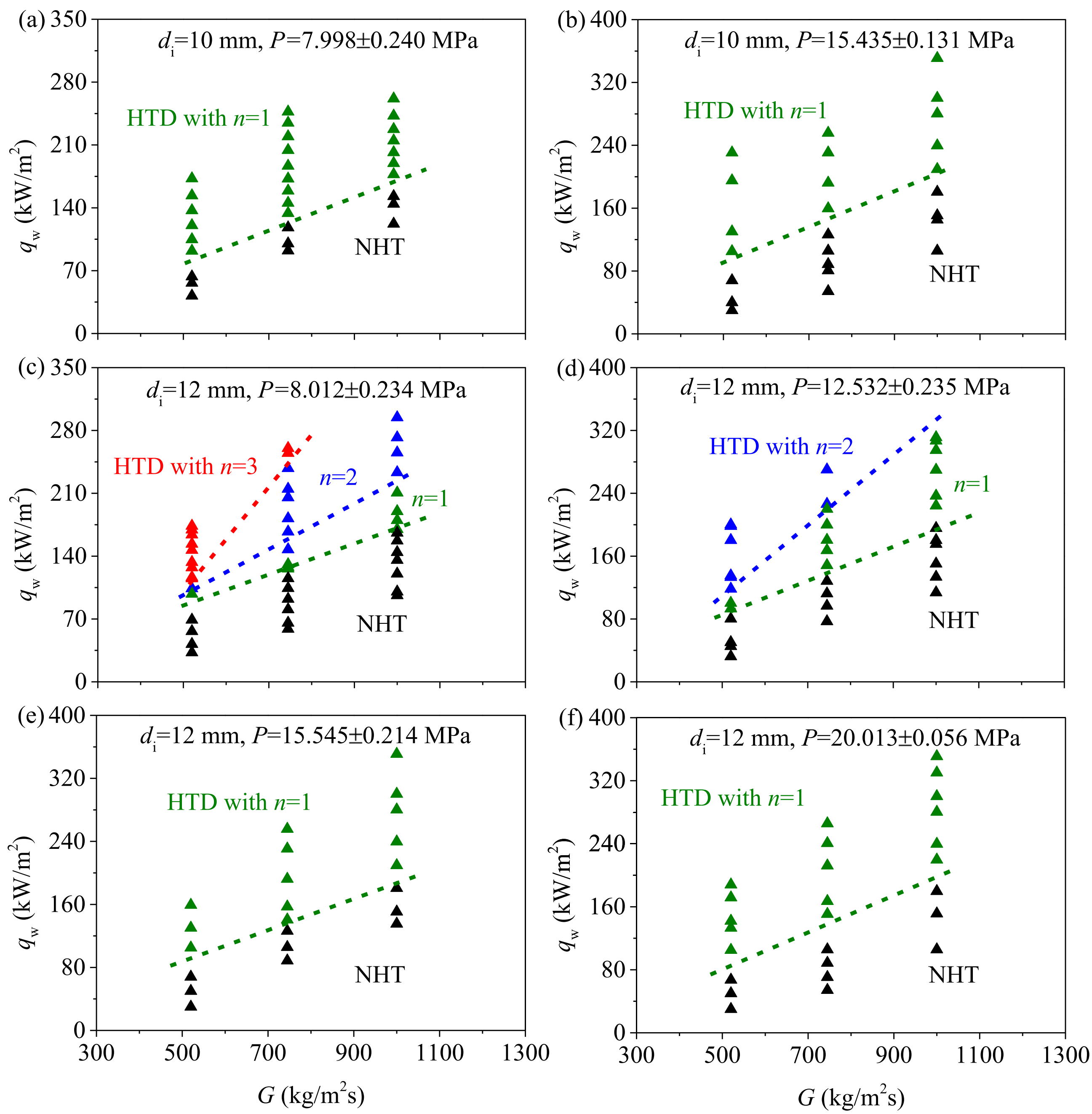

Fig. 11. Pattern maps of different heat transfer modes under different pressures for 10 mm and 12 mm tubes.

to a thickness peak of the "vapor film", which forms an "vapor" orifice as shown in Fig. 14b. For a constant mass flux m along the tube, by mass conservation,

$$m = GA_c = G_{GL}A_{GL} + G_{LL}A_{LL} \tag{23}$$

where A_c is the total cross-sectional area, G is the mass flux, subscript GL and LL represent gas-like and liquid-like phases, respectively. When the local evaporation momentum force exceeds the local inertia force, the "vapor film" near the wall starts to thicken. As the "vapor film" thickness increases gradually, the cross-sectional area occupied by "vapor film" increases, which means the area for the liquid-like phase A_{LL} becomes smaller. With a relatively unchanged liquid-vapor mass fraction, the "liquid" mass flow rate $G_{LL}A_{LL}$ remains relatively constant, and the decreased A_{LL} indicates an increased "liquid" mass flux G_{LL}. In other words, as the "two-phase" flow flows along the tube, the local small A_{LL} at the temperature peak location acts as an orifice, which contracts the bulk fluid, causing an increased "liquid" flow velocity u_{LL} and consequently an increased local inertia force at the interface ($F_{I'} = \rho_l {u_{LL}}^2$). Meanwhile, the local evaporation momentum force ($F_{M'} = (q''/i_{pc})^2/\rho_v$, where q'' is the "interfacial evaporation" heat flux) remains relatively unchanged. Therefore, after the peak, the local inertia force outweighs the local evaporation momentum force again due to the contraction effect by the orifice, which results in the reduction of the "vapor film" thickness and consequently the recovery from the HTD temperature peak. As shown in Fig. 14c, as fluid flows along the tube, initially, the local evaporation momentum force dominates, resulting in the gradual increase of the "vapor film" thickness, which causes the increase of wall temperature. With increasing "vapor film" thickness, the local inertia force gradually regains dominance, which results in the de-

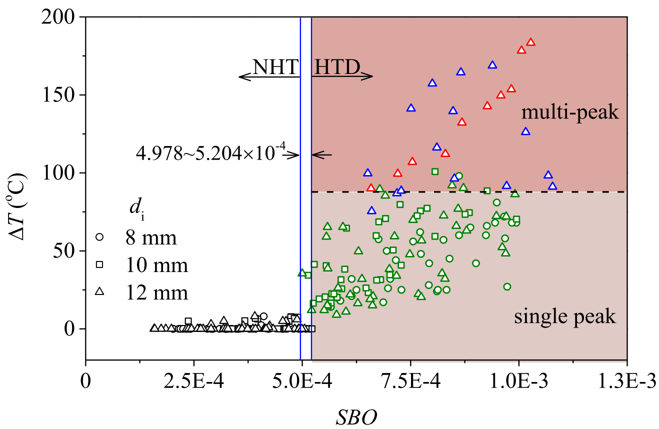

Fig. 12. Temperature rise as a function of *SBO* for both normal heat transfer (NHT) regime and heat transfer deterioration (HTD) regime. The multi-peak cases have higher temperature rise than the single-peak cases.

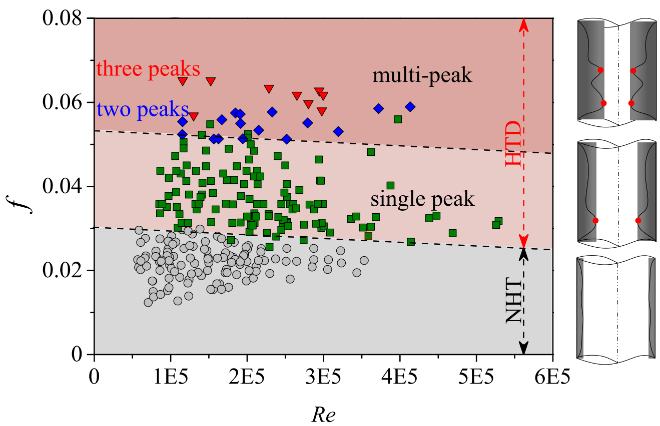

Fig. 13. Friction factors *f* versus *Re* for different heat transfer modes.

crease of the "vapor film" thickness and the recovery of wall temperature. The rise and recovery of wall temperature result in the formation of a temperature peak. It is worth noting that in our current experimental configuration, the thickness of the "vapor film" at a given axial coordinate cannot be measured, so that the cross-sectional area for liquid-like phase is not readily available. Hence, the local velocity for the liquid-like phase u_{LL} and consequently the magnitude of the local inertia force $F_{I'} = \rho_l {u_{LL}}^2$ cannot be determined. On the other hand, in the equation for the evaporation momentum force $F_{M'} = (q''/i_{pc})^2/\rho_v$, the pseudocritical enthalpy i_{pc} is a simplified replacement for the pseudo-boiling enthalpy Δi_{pb}. However, the definition of Δi_{pb} and its calculation method are not well-established. Therefore, the simplification of using i_{pc} indicates that the equation for the local $F_{M'}$ can only be used for scaling analysis.

Fig. 14d shows the wall temperature profile of a two-peak case. The two wall temperature peaks correspond to two thickness peaks of the "vapor film" as shown in Fig. 14e. Similarly, the reason for the reduction of the "vapor film" thickness after the first peak is also the increase of the local inertia force due to the orifice contraction effect. Here, after the first peak is recovered, the cross-sectional area of the liquid-like phase A_{LL} also recovers, which renders a reduced "liquid" velocity, and hence a smaller local inertia force. As qualitatively shown in Fig. 14f, this smaller local inertia force compared to the relatively unchanged local evaporation momentum force causes the "vapor film" to thicken again, thereby producing a second deterioration peak in the temperature distribution, which then recovers again due to the second orifice contraction. Therefore, the appearance of two peaks in the axial temperature profile is essentially attributed to the relatively unchanged local evaporation momentum force and the oscillating local inertia force along the tube. In other words, the local evaporation momentum force and the local inertia force obtain alternating dominance along the tube, which causes the oscillation of "vapor film" thickness and wall temperature. Moreover, when the first peak is tall enough, meaning the "vapor film" is thick enough, one orifice contraction cannot fully suppress its thickness, and the film starts to grow again because the evaporation momentum force dominates again, which recovers again later due to the contraction by the second orifice. Consequently, a second peak is formed. Similarly, for three-peak cases, after the second peak, the small local inertia force is not able to suppress the thickening of the "vapor film", causing the local evaporation momentum force to dominate again and the "vapor film" to grow again, and consequently, the third peak to appear. The formation and recovery of this third peak essentially have the same mechanisms as those of the second one. Therefore, in the three-peak cases, the local inertia force oscillates three times and there are three orifices formed along the tube.

It is worth noting that the competition between the local inertia force and local evaporation momentum force discussed above is different from the previous dimensionless analysis using *SBO*. Although *SBO* also reflects the competition between inertia force and evaporation momentum force, it focuses on global behavior, and the quantities used to calculate *SBO* are all global values as shown in Eq. (21). This is also the reason why *SBO* can only determine whether HTD occurs or not, but cannot describe the detailed behavior of HTD. However, the analysis using local inertia force and local evaporation momentum force reflects the local behavior at a given cross-section along the tube. Although the local values cannot be precisely calculated due to the lack of knowledge about the "vapor film" thickness along the tube, a qualitative understanding can be given. Moreover, experimental measurement of the "vapor film" thickness also needs to be sought for in the future, which will also enable the calculation of a local dimensionless number to describe the competition between the two local forces quantitatively. In the future, the gamma ray method and the micro-thermocouple method can be potentially used to experimentally measure the thickness of the "vapor film". When a gamma ray passes through a tube with supercritical flow inside, different "vapor film" thickness results in different total absorption property. Hence, by measuring the decay of the gamma ray, the thickness of the "vapor film" can be extracted. Alternatively, by inserting a fast response microscale thermocouple inside the tube with its radial position accurately controlled, the dynamic local temperature profile at a given radial coordinate can be measured, and the location of the "interface" can be extracted.

The difference between single-peak and multi-peak cases is essentially resulted from the difference of the deterioration magnitude, i.e., the "height" of the peak. As discussed before and shown in Fig. 12, the multi-peak cases have larger temperature rise than single-peak cases, which indicates thicker "vapor film". Therefore, the occurrence of multiple peaks is associated with a thick "vapor film" for the first peak, which cannot be recovered easily by only one orifice, and hence causes the following peaks. In other words, multiple peaks will only appear if the first temperature peak is tall enough. When the first peak is short, the "vapor film" is relatively thin, and its thickness can be stabilized after one orifice contraction. This conclusion can also explain why the multi-peak cases were only observed in the 12 mm tube but not in the 8 mm and 10 mm tubes: with a larger tube diameter, there is more room and higher possibility for the "vapor film" to grow and reach a large thickness to induce multiple peaks. Future study is needed

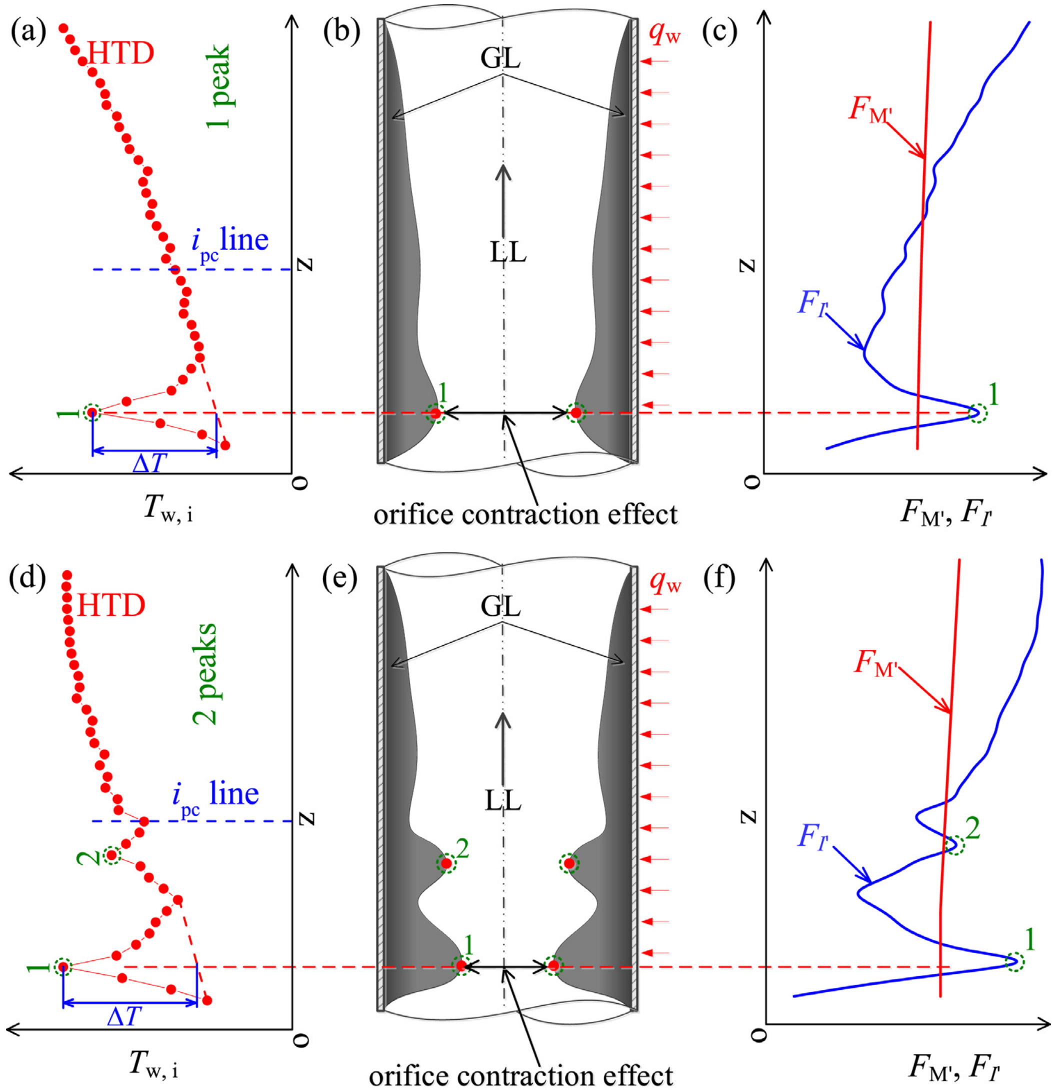

Fig. 14. Schematics showing the mechanisms for single-peak (a-c) and two-peak (d-f) cases. (a) Wall temperature profile of a single-peak case. (b) Schematic showing the formation of a "vapor" orifice at the peak for the single-peak case. (c) Schematic showing the qualitative variation of evaporation momentum force and inertia force along the tube for the single-peak case. (d) Wall temperature profile of a two-peak case. (b) Schematic showing the formation of two "vapor" orifices at the peaks for the two-peak case. (c) Schematic showing the qualitative variation of evaporation momentum force and inertia force along the tube for the two-peak case.

to investigate the "vapor film" thickness during supercritical heat transfer, especially comparison between the thicknesses at a temperature peak and after the peak.

4. Conclusions

In this work, heat transfer of supercritical CO_2 flowing upward inside vertical heated tubes was experimentally studied. The experimental working pressure, mass flux, and wall heat flux covered the ranges of 7.5~23 MPa, 400~1500 kg/m^{2}s, and 25~450 kW/m^2, respectively, and tubes with inner diameter of 8 mm, 10 mm, and 12 mm were used. The main conclusions of this paper are listed as follows:

1) Variation of tube diameter affects the heat transfer characteristics of supercritical CO_2. Under the same working conditions, the heat transfer coefficient decreases with increasing tube diameter. The reason is because larger tube diameter causes smaller velocity gradient near the tube wall and consequently smaller inertia force acting on the "vapor film", resulting in worse heat transfer. The effect of tube diameter on heat transfer diminishes at high pressures, because the difference between liquid-like and gas-like phases diminishes.
2) For the three tubes studied in this work, variation of tube diameter does not affect the transition boundary between NHT and HTD. *SBO* serves as the critical parameter distinguishing NHT and HTD regimes, which is proposed based on the pseudo-boiling theory and represents the competition between the global evaporation momentum force and inertia force. For different tube diameters, the critical *SBO* is relatively unchanged, in the range of $4.978 \sim 5.204 \times 10^{-4}$.
3) In the HTD regime, three different types of deterioration are observed in the 12 mm tube: with single peak, two peaks, and three peaks in the temperature profiles. The multi-peak phenomenon has higher temperature rise than single-peak cases, indicating that thicker "vapor film" at the first peak is the reason causing the multi-peak phenomenon. Large tube diameter results in small velocity gradient near the wall, which causes thick "vapor film". At high pressures, the "vapor film" is thinner due to the smaller expansion coefficient of the gas-like phase. Thus, multi-peak phenomenon occurs with large tube diameter and under low pressure.

4) The mechanism causing the multi-peak phenomenon is the orifice contraction effect. Different from the global parameter *SBO*, competition between the local evaporation momentum force and inertia force determines the local heat transfer. Each peak corresponds to the formation of an "vapor orifice", which results in higher friction factor for multi-peak cases compared with single-peak cases due to the existence of multiple orifices. When local evaporation momentum force dominates, the "vapor film" starts to grow and form an orifice. Contraction effect of the orifice increases the local inertia force and results in reduction of "vapor film" thickness and recovery from wall temperature peak. When the first peak corresponds to large "vapor film" thickness, the thick film cannot be suppressed by one contraction event, and oscillation of the local inertia force causes the formation of multiple peaks.

Declaration of Competing Interest

The authors declare that they have no known competing financial interests or personal relationships that could have appeared to influence the work reported in this paper.

CRediT authorship contribution statement

Haisong Zhang: Conceptualization, Investigation, Writing – original draft. **Jinliang Xu:** Supervision, Project administration, Funding acquisition, Writing – review & editing. **Qingyang Wang:** Conceptualization, Visualization, Writing – original draft, Writing – review & editing. **Xinjie Zhu:** Investigation, Validation.

Acknowledgements

The study was supported by the National Natural Science Foundation of China (51821004).

References

[1] Ž. Knez, E. Markočič, M. Leitgeb, M. Primožič, M. Knez Hrnčič, M. Škerget, Industrial applications of supercritical fluids: A review, Energy 77 (2014) 235–243.
[2] D. Bolmatov, V.V. Brazhkin, K. Trachenko, Thermodynamic behaviour of supercritical matter, Nature Communications 4 (1) (2013) 2331.
[3] L. Cheng, G. Ribatski, J.R. Thome, Analysis of supercritical CO2 cooling in macro-and micro-channels, International journal of refrigeration 31 (8) (2008) 1301–1316.
[4] W.H. Stein, R. Buck, Advanced power cycles for concentrated solar power, Solar Energy 152 (2017) 91–105.
[5] Y. Yang, W. Bai, Y. Wang, Y. Zhang, H. Li, M. Yao, H. Wang, Coupled simulation of the combustion and fluid heating of a 300 MW supercritical CO2 boiler, Applied Thermal Engineering 113 (2017) 259–267.
[6] Z. Zhang, R. Zhou, X. Ge, J. Zhang, X. Wu, Perspectives for 700 °C ultra-supercritical power generation: Thermal safety of high-temperature heating surfaces, Energy 190 (2020) 116411.
[7] J. Xu, E. Sun, M. Li, H. Liu, B. Zhu, Key issues and solution strategies for supercritical carbon dioxide coal fired power plant, Energy 157 (2018) 227–246.
[8] J. Xu, C. Liu, E. Sun, J. Xie, M. Li, Y. Yang, J. Liu, Perspective of S− CO2 power cycles, Energy 186 (2019) 115831.
[9] D. Yang, G. Tang, Y. Fan, X. Li, S. Wang, Arrangement and three-dimensional analysis of cooling wall in 1000 MW S–CO2 coal-fired boiler, Energy 197 (2020) 117168.
[10] Y. Ahn, S.J. Bae, M. Kim, S.K. Cho, S. Baik, J.I. Lee, J.E. Cha, Review of supercritical CO2 power cycle technology and current status of research and development, Nuclear Engineering and Technology 47 (6) (2015) 647–661.
[11] E. Sun, J. Xu, M. Li, G. Liu, B. Zhu, Connected-top-bottom-cycle to cascade utilize flue gas heat for supercritical carbon dioxide coal fired power plant, Energy Conversion and Management 172 (2018) 138–154.
[12] J. Sarkar, S. Bhattacharyya, Optimization of recompression S-CO2 power cycle with reheating, Energy Conversion and Management 50 (8) (2009) 1939–1945.
[13] M. Pizzarelli, The status of the research on the heat transfer deterioration in supercritical fluids: A review, International Communications in Heat and Mass Transfer 95 (2018) 132–138.
[14] Q. Zhang, H. Li, X. Lei, J. Zhang, X. Kong, Study on identification method of heat transfer deterioration of supercritical fluids in vertically heated tubes, International Journal of Heat and Mass Transfer 127 (2018) 674–686.
[15] X. Cheng, X. Liu, Research challenges of heat transfer to supercritical fluids, Journal of Nuclear Engineering and Radiation Science 4 (1) (2018).
[16] D. Huang, Z. Wu, B. Sunden, W. Li, A brief review on convection heat transfer of fluids at supercritical pressures in tubes and the recent progress, Applied Energy 162 (2016) 494–505.
[17] W. Chen, X. Fang, A new heat transfer correlation for supercritical water flowing in vertical tubes, International Journal of Heat and Mass Transfer 78 (2014) 156–160.
[18] D. Huang, W. Li, A brief review on the buoyancy criteria for supercritical fluids, Applied Thermal Engineering 131 (2018) 977–987.
[19] B. Shiralkar, P. Griffith, The effect of swirl, inlet conditions, flow direction, and tube diameter on the heat transfer to fluids at supercritical pressure, Journal of Heat Transfer 92 (3) (1970) 465–471.
[20] J. Jackson, W. Hall, J. Fewster, A. Watson, M. Watts, in: Heat transfer to supercritical pressure fluids, UKAEA, AERER, 1975, p. 8158.
[21] J. Jackson, M. Cotton, B. Axcell, Studies of mixed convection in vertical tubes, International journal of heat and fluid flow 10 (1) (1989) 2–15.
[22] S. Liu, Y. Huang, G. Liu, J. Wang, L.K. Leung, Improvement of buoyancy and acceleration parameters for forced and mixed convective heat transfer to supercritical fluids flowing in vertical tubes, International Journal of Heat and Mass Transfer 106 (2017) 1144–1156.
[23] D.E. Kim, M.H. Kim, Experimental study of the effects of flow acceleration and buoyancy on heat transfer in a supercritical fluid flow in a circular tube, Nuclear Engineering and Design 240 (10) (2010) 3336–3349.
[24] D. McEligot, C. Coon, H. Perkins, Relaminarization in tubes, International Journal of Heat and Mass Transfer 13 (2) (1970) 431–433.
[25] H. Wang, L.K. Leung, W. Wang, Q. Bi, A review on recent heat transfer studies to supercritical pressure water in channels, Applied Thermal Engineering 142 (2018) 573–596.
[26] J. Peeters, R. Pecnik, M. Rohde, T. van der Hagen, B.J. Boersma, Characteristics of turbulent heat transfer in an annulus at supercritical pressure, Physical Review Fluids 2 (2) (2017) 024602.
[27] K. Kim, J.-P. Hickey, C. Scalo, Pseudophase change effects in turbulent channel flow under transcritical temperature conditions, Journal of Fluid Mechanics 871 (2019) 52–91.
[28] G. Simeoni, T. Bryk, F. Gorelli, M. Krisch, G. Ruocco, M. Santoro, T. Scopigno, The Widom line as the crossover between liquid-like and gas-like behaviour in supercritical fluids, Nature Physics 6 (7) (2010) 503–507.
[29] P. Gallo, D. Corradini, M. Rovere, Widom line and dynamical crossovers as routes to understand supercritical water, Nature communications 5 (1) (2014) 1–6.
[30] D. Banuti, Crossing the Widom-line–Supercritical pseudo-boiling, The Journal of Supercritical Fluids 98 (2015) 12–16.
[31] F. Maxim, C. Contescu, P. Boillat, B. Niceno, K. Karalis, A. Testino, C. Ludwig, Visualization of supercritical water pseudo-boiling at Widom line crossover, Nature communications 10 (1) (2019) 1–11.
[32] J. Tamba, T. Ohara, T. Aihara, MD study on interfacelike phenomena in supercritical fluid, Microscale Thermophysical Engineering 1 (1) (1997) 19–30.
[33] B. Zhu, J. Xu, X. Wu, J. Xie, M. Li, Supercritical "boiling" number, a new parameter to distinguish two regimes of carbon dioxide heat transfer in tubes, International Journal of Thermal Sciences 136 (2019) 254–266.
[34] J. Xu, H. Zhang, B. Zhu, J. Xie, Critical supercritical-boiling-number to determine the onset of heat transfer deterioration for supercritical fluids, Solar Energy 195 (2020) 27–36.
[35] B. Zhu, J. Xu, H. Zhang, J. Xie, M. Li, Effect of non-uniform heating on scCO2 heat transfer deterioration, Applied Thermal Engineering 181 (2020) 115967.
[36] B. Zhu, J. Xu, C. Yan, J. Xie, The general supercritical heat transfer correlation for vertical up-flow tubes: K number correlation, International Journal of Heat and Mass Transfer 148 (2020) 119080.
[37] H. Zhang, J. Xu, X. Zhu, J. Xie, M. Li, B. Zhu, The K number, a new analogy criterion number to connect pressure drop and heat transfer of sCO2 in vertical tubes, Applied Thermal Engineering (2020) 116078.
[38] P. Bourke, D. Pulling, L. Gill, W. Denton, Forced convective heat transfer to turbulent CO2 in the supercritical region, International journal of heat and mass transfer 13 (8) (1970) 1339–1348.
[39] J. Ackerman, Pseudoboiling heat transfer to supercritical pressure water in smooth and ribbed tubes, Journal of Heat Transfer 92 (3) (1970) 490–497.
[40] J. Jackson, K. Lutterodt, R. Weinberg, Experimental studies of buoyancy-influenced convective heat transfer in heated vertical tubes at pressures just above and just below the thermodynamic critical value, in: Proceedings of the Joint International Conference on Global Environment and Nuclear Energy System/Advanced Power Plants, 2003, pp. 15–19.
[41] H. Cheng, J. Zhao, M.K. Rowinski, Study on two wall temperature peaks of supercritical fluid mixed convective heat transfer in circular tubes, International Journal of Heat and Mass Transfer 113 (2017) 257–267.
[42] Z. Luo, X. Fang, Y. Yang, W. Chen, L. Zhang, Prediction of "critical heat flux" for supercritical water and CO2 flowing upward in vertical heated tubes, International Journal of Heat and Mass Transfer 159 (2020) 120115.
[43] S.G. Kandlikar, Heat transfer mechanisms during flow boiling in microchannels, J. Heat Transfer 126 (1) (2004) 8–16.
[44] D. Kandlikar, G. Satish, Evaporation Momentum Force and Its Relevance to Boiling Heat Transfer, Journal of Heat Transfer (2020).
[45] R.-N. Xu, F. Luo, P.-X. Jiang, Buoyancy effects on turbulent heat transfer of supercritical CO2 in a vertical mini-tube based on continuous wall temperature measurements, International journal of heat and mass transfer 110 (2017) 576–586.